Atmospheric Environment 88 (2014) 308–319

Contents lists available at ScienceDirect

Atmospheric Environment

journal homepage: www.elsevier.com/locate/atmosenv

Measurements of submicron aerosols at the California–Mexico border during the Cal–Mex 2010 field campaign

Misti E. Levy [a], Renyi Zhang [a, b, *], Jun Zheng [a, c], Haobo Tan [d], Yuan Wang [a], Luisa T. Molina [e], S. Takahama [f, g], L.M. Russell [f], Guohui Li [h]

[a] Department of Atmospheric Sciences, Center for Atmospheric Chemistry and Environment, Texas A&M University, College Station, TX 77843, USA
[b] Department of Chemistry, Center for Atmospheric Chemistry and Environment, Texas A&M University, College Station, TX 77843, USA
[c] School of Environmental Science and Engineering, Nanjing University of Information Science & Technology, Nanjing 210044, PR China
[d] Institute of Tropical and Marine Meteorology, CMA, Guangdong 510080, PR China
[e] Molina Center for Energy and the Environment, La Jolla, CA 92037, USA
[f] Scripps Institution of Oceanography, University of California San Diego, La Jolla, CA 92093-0221, USA
[g] EPFL ENAC IIE APRL, GR C1 537 (Bâtiment GR), Station 2, CH-1015 Lausanne, Switzerland
[h] Institute of Earth Environment, Chinese Academy of Sciences, No 10 Fenghui South Road, Xi'an High-Tech Zone, 710075 Xi'an, PR China

HIGHLIGHTS

- Comprehensive measurements of aerosol properties during the Cal–Mex 2010 study.
- An average black carbon mass concentration of 2.87 ± 2.65 μg m^{-3}.
- Gasoline and diesel vehicles produce a significant amount of BC particles.

ARTICLE INFO

Article history:
Received 27 June 2013
Received in revised form
23 August 2013
Accepted 28 August 2013
Available online 21 September 2013

Keywords:
Air pollution
Aerosol
Black carbon
Border region
US
Mexico

ABSTRACT

We present measurements of submicron aerosols in Tijuana, Mexico during the Cal–Mex 2010 field campaign. A suite of aerosol instrumentations were deployed, including a hygroscopic–volatility tandem differential mobility analyzer (HV–TDMA), aerosol particle mass analyzer (APM), condensation particle counter (CPC), cavity ring-down spectrometer (CRDS), and nephelometer to measure the aerosol size distributions, effective density, hygroscopic growth factors (HGF), volatility growth factors (VGF), and optical properties. The average mass concentration of $PM_{0.6}$ is 10.39 ± 7.61 μg m^{-3}, and the derived average black carbon (BC) mass concentration is 2.87 ± 2.65 μg m^{-3}. There is little new particle formation or particle growth during the day, and the mass loading is dominated by organic aerosols and BC, which on average are 37% and 27% of $PM_{1.0}$, respectively. For four particle sizes of 46, 81, 151, and 240 nm, the measured particle effective density, HGFs, and VGFs exhibit distinct diurnal trends and size-dependence. For smaller particles (46 and 81 nm), the effective density distribution is unimodal during the day and night, signifying an internally mixed aerosol composition. In contrast, larger particles (151 and 240 nm) exhibit a bi-modal effective density distribution during the daytime, indicating an external mixture of fresh BC and organic aerosols, but a unimodal distribution during the night, corresponding to an internal mixture of BC and organic aerosols. The smaller particles show a noticeable diurnal trend in the effective density distribution, with the highest effective density (1.70 g cm^{-3}) occurring shortly after midnight and the lowest value (0.90 g cm^{-3}) occurring during the afternoon, corresponding most likely to primary organic aerosols and BC, respectively. Both HGFs and VGFs measured are strongly size-dependent. HGFs increase with increasing particle size, indicating that the largest particles are more hygroscopic. VGFs decrease with increasing particle size, indicating that larger particles are more volatile. The hygroscopicity distributions of smaller particles (46 and 81 nm) are unimodal, with a HGF value close to unity. Large particles typically exhibit a bi-modal distribution, with a non-hygroscopic mode and a hygroscopic mode. For all particle sizes, the VGF distributions are bimodal, with a primary non-volatile mode and a secondary volatile mode. The average extinction, scattering, and

---

* Corresponding author. Department of Atmospheric Sciences, Center for Atmospheric Chemistry and Environment, Texas A&M University, College Station, TX 77843, USA.
E-mail address: renyi-zhang@tamu.edu (R. Zhang).

1352-2310/$ – see front matter Published by Elsevier Ltd.
http://dx.doi.org/10.1016/j.atmosenv.2013.08.062

absorption coefficients are 86.04, 63.07, and 22.97 Mm^{-1}, respectively, and the average SSA is 0.75. Our results reveal that gasoline and diesel vehicles produce a significant amount of black carbon particles in this US–Mexico border region, which impacts the regional environment and climate.

1. Introduction

Tijuana, Mexico is located near San Diego at the United States–Mexico border (Fig. 1). There are two international ports in Tijuana, San Ysidro and Otay Mesas, through which more than 50 million people pass each year (Border 2012, 2005). Since the enactment of the North American Free Trade Agreement (NAFTA) in 1993, the United States–Mexico border regions have experienced rapid growth in population, maquiladoras (manufacturing plants within the free trade zone), and cross-border transportation. This growth has been especially prevalent in the Tijuana region, where the population approximately was doubled between 1990 and 2010 (Border, 2012, 2011; Brinkhoff, 2012). The peak concentration of Mexican maquiladoras occurred in Tijuana in 2001, with 820 simultaneously operating maquiladoras (Center of Information for Men and Women Workers, 2004). However, this economic development has been coupled with an undesirable environmental impact.

There has been an increased governmental response to the environmental conditions in this region. Border 2012 was a bi-national program started in 2002 that focused on protecting the environment, public health, and sustainable development (Border, 2012, 2011). This program has been succeeded by Border 2020, which focuses on decision-making, priority setting, and addressing the environmental and public health strains (Border, 2020, 2012).

Two large-scale research endeavors have been conducted near the California–Mexico border, the 1997 Southern California Ozone Study (SCOS97) and Cal–Mex 2010. SCOS97, conducted in 1997, analyzed a broad range of atmospheric constituents and air quality indicators (Croes and Fujita, 2003; Zielinska and Fujita, 2003). The Cal–Mex 2010 field campaign collected a detailed data set of gaseous and particulate matter (PM) pollutants with the intent to provide scientific expertise for future air quality and climate change decision-making (Bei et al., 2013). The Cal–Mex 2010 was an intensive field study of emissions in the U.S.–Mexico border cities of San Diego–Tijuana and Calexico–Mexicali. This bi-national venture sought to characterize the sources of PM and precursor gases, with the intent to study their transformation, transportation, and impact on local air quality and climate. Historically, the region has exceeded both the US Environmental Protection Agency (EPA) National Ambient Air Quality Standards (NAAQS) and Mexico's Secretaria del Medio Ambiente Recursos Naturales (SEMARNAT) air standards, stimulating a bi-nation interest. Mexican cities generally have a much higher exceedance rate of the PM standard than its US counterparts. For example, between 2005 and 2007, San Diego exceeded the EPA's and SEMARNAT's 24 h PM_{10} standards (both 150 $\mu\mathrm{g\ m}^{-3}$) on 15 occasions compared to 223 cases exceeded in Tijuana (EPA/CICA online data). This disproportionate distribution of pollutants between the two neighboring US–Mexico cities was also observed in Calexico–Mexicali (Chow et al., 2000) and in El Paso–Ciudad Juarez (Kelly et al., 2006). Several studies have been conducted in this region examining nitrogen oxides (NO_x), volatile organic compounds (VOCs) (Zielinska and Fujita, 2003; Zheng et al., 2013b), ozone (Shi et al., 2009; Wang et al., 2009), organic aerosols (Takahama et al., 2013), black carbon (BC) (Kelly et al., 2006; Shores et al., 2013), and PM transportation and concentration (Chow et al., 2000; Mendoza et al., 2010). Photochemical oxidation of VOCs in the presence of NO_x not only contributes to ozone formation (Nesbitt et al., 2000; Bond et al., 2002; Zhang et al., 2004a), but is also responsible for secondary organic aerosol formation (Zhang, 2010; Zhang et al., 2012). A comprehensive study of the properties of ambient aerosols in this region has yet to be reported.

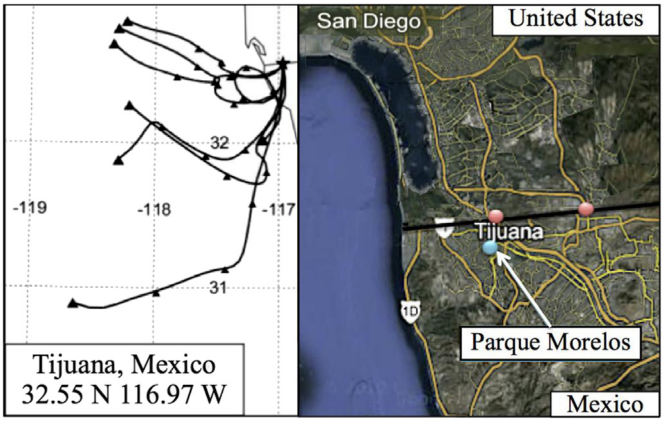

Fig. 1. Map of Tijuana, Baja California, Mexico and back-trajectories using the NOAA–HYSPLIT model to demonstrate the synoptic flow commonly observed during Cal–Mex 2010. The back-trajectories shown correspond to 31 May–07 June 2010.

Aerosols, formed from natural and anthropogenic sources, exert profound impacts on the Earth–atmosphere system. For example, aerosols influence the climate directly by reflecting solar radiation (Haywood and Boucher, 2000; Ramanathan et al., 2001; Forster et al., 2007; Zhang et al., 2007), indirectly by modifying cloud formation (Fan et al., 2007, 2008), modulating photochemistry (Li et al., 2005), and promoting multiphase chemistry (Zhang et al., 1996a; Molina et al., 1997; Zhao et al., 2005a,b). Elevated aerosol concentrations are a principal contributor to air pollution and have negative impacts on human health, which are major concerns in the region (Mokdad et al., 2004; Dominici et al., 2006). The degree of aerosol impacts is dependent on their concentration, size, and chemical composition (Wang et al., 2010a,b).

In this paper, we report measurements of ambient aerosol properties conducted in Tijuana, Mexico, between 15 May and 30 June 2010. The particle size distribution, number concentration, volatility (VGF) and hygroscopic (HGF) growth factors, effective density, and optical properties were concurrently measured by a suite of aerosol instrumentations, to evaluate the formation, transformation, and properties of submicron aerosols in this region.

2. Methodology and instrumentation

The measurement site was located in Parque Morelos, near the center of Tijuana, Baja California, Mexico. The instruments were placed in an air-conditioned trailer. Measurements of aerosol optical properties, effective density, and size distribution were made simultaneously. Ambient aerosols were sampled at 10 L per minute through a 6 m thermally insulated copper tube (3/8″). The aerosols were then passed through several Nafion driers (PD-070-18T-24SS, Perma Pure, Inc.) to reduce the relative humidity to 10%.

A Differential Mobility Analyzer (DMA, model 3081, TSI, Inc.), an Aerosol Particle Mass analyzer (APM, model 3600, Kanomax Inc., Japan), and a Condensation Particle Counter (CPC, model 3760A, TSI, Inc.) were used to obtain the particle size distribution and effective density. When calculating the particle size distributions, diffusion-controlled particle losses in the driers were accounted using an inversion algorithm. A detailed description of this aerosol operating system has been provided previously (Khalizov et al., 2009a; Pagels et al., 2009; Xue et al., 2009a,b). Each DMA–APM–CPC cycle observed a single size distribution from 20 to 600 nm and followed by effective density measurements for four particle diameters, which required approximately one hour to complete. The particle effective density was calculated for four mobility diameters (46, 81, 151, and 240 nm) from the DMA–APM measurements,

$$\rho_{\mathrm{eff}} = V_{\mathrm{APM}}/V_{\mathrm{APM,PSL}} \times \rho_{\mathrm{PSL}} \quad (1)$$

where V_{APM} and $V_{\mathrm{APM,PSL}}$ are the peak APM voltages corresponding to the masses of ambient and polystyrene latex (PSL) particles, respectively, which are unique to each mobility diameter. The material density of polystyrene latex is $\rho_{\mathrm{PSL}} = 1.054\ \mathrm{g\ cm^{-3}}$. The values for $V_{\mathrm{APM,PSL}}$ and V_{APM} for each mobility diameter are summarized in Table 1.

A Hygroscopic–Volatility Tandem DMA (HV–TDMA) was used to determine the size resolved HGF and VGF distributions. During hygroscopicity measurements, monodisperse aerosols produced by the first DMA were exposed to elevated humidity (~90%). As previous studies have focused on the effects of increased humidity on atmospheric particles (Swietlicki et al., 2008; Khalizov et al., 2009b; Massoli et al., 2009; Meier et al., 2009), we determined the aerosol composition for our observational period on the basis of the previous studies. In our volatility measurements, the monodisperse aerosols were exposed to increased temperatures (350 °C). Most compounds volatilized at a characteristic temperature, and by knowing the temperature we can deduce the remaining composition after heat exposure (Villani et al., 2007). After exposure to temperatures near 350 °C, the remaining mass would be composed of non-volatile materials, such as elemental carbon, crustal material, sea salt, or char. Since both the hygroscopicity and volatility routines alter the particle size due to hygroscopic growth or loss of volatile materials, respectively, the particle were passed through the second DMA to measure the changes in mobility diameters (Gasparini et al., 2004; Khalizov et al., 2009b). The growth factor was determined by the ratio of the initial dry particle diameter, D_{o}, and the processed diameter, D_{p},

$$\text{HGF or VGF} = D_{\mathrm{P}}/D_{\mathrm{o}} \quad (2)$$

Optical measurements were carried out concurrently with a two-minute temporal resolution. Aerosol extinction coefficients were measured at 532 nm with a Cavity Ring-Down Spectrometer (CRDS) (Smith and Atkinson, 2001; Khalizov et al., 2009a; Radney et al., 2009). Scattering coefficients at 532 nm were derived from measurements by a commercial three-wavelength (450, 550, and 700 nm) integrating nephelometer (TSI 3563) (Anderson and Ogren, 1998). Losses of optically important particles were estimated to be less than 1%, and the detection sensitivity of this instrument was better than 0.5 $\mathrm{Mm^{-1}}$. From the extinction and scattering coefficients, the single scattering albedo (SSA) and the absorption coefficients were calculated. The SSA is the ratio of the scattering coefficients to the extinction coefficients, and the absorption (Abs) coefficient is the difference of the extinction (Ext) and scattering (Sca) coefficients,

Table 1
The values for $V_{\mathrm{APM,PSL}}$ and V_{APM} for each mobility diameter in the DMA–APM settings.

Mobility diameter	V_{APM}	RPM	$V_{\mathrm{APM,PSL}}$
46 nm	295	7000	21.9
81 nm	774	5000	57.3
151 nm	2111.8	5000	346.8
240 nm	4275.2	3500	671.3

$$\mathrm{SSA} = \mathrm{Sct}/\mathrm{Ext} \quad (3)$$

The detection limit for absorption using the difference method was within 0.6 $\mathrm{Mm^{-1}}$, on the basis of laboratory calibration (Khalizov et al., 2009a, 2013; Xue et al., 2009b).

From measured size-resolved effective densities and number size distributions, the mass concentration of particles between 20 and 600 nm was estimated, shown as $\mathrm{PM_{0.6}}$ (particulate matter smaller than 600 nm in diameter),

$$\mathrm{PM_{0.6}} = \int_{20\ \mathrm{nm}}^{600\ \mathrm{nm}} \frac{1}{6} \times \mathrm{d}N \times \pi \times D_{\mathrm{o}}^{3} \times \rho_{\mathrm{eff}} \times \Delta D_{\mathrm{o}} \quad (4)$$

In addition to the calculated $\mathrm{PM_{0.6}}$ concentration, aerosol composition data was also collected by an Aerosol Chemical Speciation Monitor (ACSM). The ACSM is a simplified Aerodyne Aerosol Mass Spectrometer (AMS) without the time-of-flight measurements (Takahama et al., 2013), which measures the non-refractory $\mathrm{PM_{1.0}}$ aerosol total mass loadings and chemical composition of ammonium, sulfate, organics, nitrate, and chloride in thirty-minute cycles (Sun et al., 2013). The ACSM was equipped with a Pfeiffer Prisma quadrupole mass spectrometer with a time resolution of 15–30 min. Since the ACSM system measures non-refractory aerosols, sea salt and mineral dust are excluded; a detailed description of ACSM has been previously reported elsewhere (Ng et al., 2011; Aiken et al., 2010; Takahama et al., 2013).

The mass concentration of BC was calculated by two independent approaches. The concentration of BC (Opt_BC) was derived from the light absorption coefficients, assuming uniform values of the mass absorption cross-section (MAC) of 7.5 and 11 $\mathrm{cm^{2}\ g^{-1}}$ for fresh and aged BC, respectively (Bond and Bergstrom, 2006),

$$\mathrm{Opt\_BC} = \mathrm{Abs}/\mathrm{MAC} \quad (5)$$

The appropriate MAC value was selected by using the photochemical age as a proxy for the mixing state of particles,

$$\text{Photochemical Age} = 1 - \mathrm{NO}_{x}/\mathrm{NO}_{y} \quad (6)$$

where NO_x and NO_y are the summations of NO and $\mathrm{NO_2}$ and the total reactive oxidized nitrogen, respectively. The absolute error in the BC mass concentration due to uncertainties in MAC and b_{abs} was estimated to be within 0.21 $\mathrm{mg\ m^{-1}}$.

Using the number concentration and the volatility measurements, we derived an alternative BC concentration (referred to as Vol_BC) for comparison. Assuming that the remaining mass was composed of predominantly BC, the remaining mass after thermal denuding in each VGF cycle was multiplied by the corresponding total number concentration to obtain the Vol_BC. The aerosol number concentration was determined from the size distributions during the same period.

3. Results and discussions

3.1. Meteorological conditions

During the field campaign, the weather pattern was predominantly clear and sunny. The back trajectories for the period of 31 May–07 June 2010 are shown in Fig. 1, depicting the synoptic flow commonly observed during the Cal–Mex 2010. The air mainly originated from the Pacific Ocean, carrying relatively clean marine masses to this region. The maximum temperature each day was near 21 °C (70 °F), and the minimum temperature was near 14 °C (56 °F). The wind frequently came from the south during the early mornings (1–6 am) and from the west/north west during the remaining portion of day. Overnight, the winds were light, and the winds peaked near noontime. There were little meteorological events during the entire field campaign. A detailed description of the meteorology during the campaign can be found in Bei et al. (2013).

3.2. Aerosol size distributions

The size-resolved aerosol number concentration and the normalized aerosol size distributions are shown in Fig. 2A and B, respectively. The normalized plot is produced by dividing each aerosol size distribution (consisting of approximately 150 points between 20 and 600 nm) by the greatest concentration in each distribution, illustrating the progression of the particle mobility diameters throughout a day. The average number concentration is 26,300 ± 15,300 particles cm^{-3} (one standard deviations). Overall, the aerosol concentration rises sharply near sunrise, remains elevated throughout the day, and decrease overnight (after 10 pm). The highest concentrations are observed for aerosols between 20 and 75 nm, which is characteristic of vehicle emissions (Ban-Weiss et al., 2010). Atmospheric new particle formation and subsequent growth of freshly nucleated particles represent a prominent feature in many polluted urban environments (Yue et al., 2010). However, there appears to exist little characteristics of new particle formation in this region. The lack of new particle formation is potentially attributable to low concentrations of gaseous SO_2 and VOCs (Zhang et al., 1996b; Zheng et al., 2013b), which enhance the nucleation and growth rates of nanoparticles (Zhang et al., 2004b, 2009), consistent with the low level of PM SO_4 (Fig. 3). Fig. 2B shows that the peak particle concentration during the daytime is consistently below 50 nm. The nighttime concentration of smaller particles (<50 nm) is approximately 20% of the daytime, and the nighttime particles are mainly greater than 50 nm. These particles can be explained by emissions of primary organic aerosols or aged primary particles coated with organic materials, to be discussed below.

Given the substantial cross-border transportation, it is reasonable to attribute the significant daytime increase in particle concentrations to vehicle emissions. Gasoline and diesel engine emissions have been found to be major sources of air pollution in this region (Zheng et al., 2013b) and significant contributors to the high BC concentration (Takahama et al., 2013). Interestingly, the weekends (i.e., 4–6 June) have a slightly different diurnal trend in the particle size distribution. On Fridays (04 June), the afternoon concentration is greater and the total concentration is elevated until after midnight. Previous studies have shown that on Friday and Saturday nights there is on average 2–3 times more cars and pedestrians crossing the border between midnight and 4 am compared to the nights of weekdays (Lange et al., 1999). This after midnight increase is also evident, but to a lesser extend on 05 June. There are overall lessened particle concentrations on Sunday (06 June), particularly in the afternoon hours.

Table 2 summarizes the averaged particle properties during the Cal–Mex 2010 field campaign.

3.3. Chemical compositions

The ACSM mass concentrations of ammonium, sulfate, organics, nitrate, and chloride and the Opt_BC concentration calculated from Equation (5) are shown in Fig. 3. It is evident that the chemical composition is mainly composed of organic aerosols (3.54 μg m^{-3} or 37%) and Opt_BC (2.87 μg m^{-3} or 27%), with lesser contributions from NO_3 (1.64 μg m^{-3} or 14%), SO_4 (0.81 μg m^{-3} or 10%), NH_4 (0.92 μg m^{-3} or 9%), and chloride (0.24 μg m^{-3} or 3%). Similar to the number size distributions, the highest mass loadings are observed in the daytime, and the lowest mass loadings are observed overnight. Given the little biogenic contribution in this region, industrial and vehicle emissions are the major contributors to the organic mass (Zheng et al., 2013a, b). Industrial, vehicle, and diesel truck emissions are also likely the main contributors to the nitrate mass loading in this region (Zheng et al., 2013a, b). The average Opt_BC concentration is 2.87 ± 2.65 μg m^{-3}, accounting for 27.41% ± 9.44 of the total $PM_{1.0}$ on average, but on several occasions the BC content accounts for over 50% of the aerosol mass loading. The BC

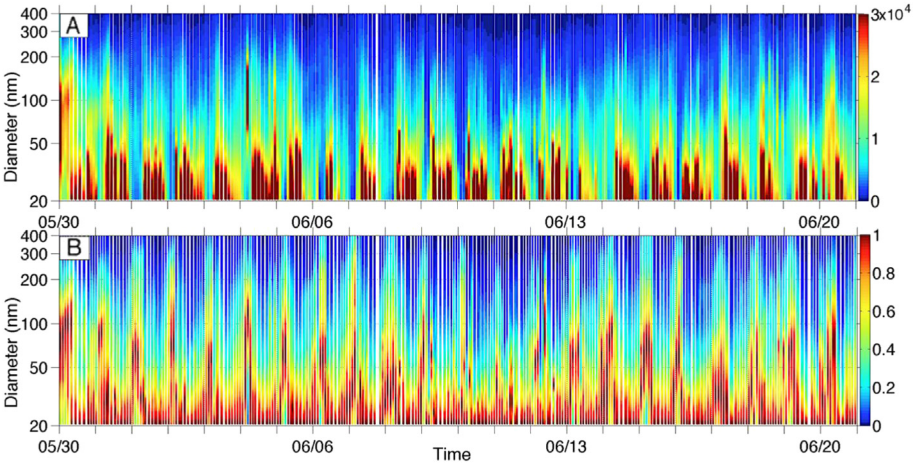

Fig. 2. Aerosol mobility size distributions: (A) Absolute number concentration (cm^{-3}) of 20–400 nm diameter particles during the entire field observational period. The dates marked correspond to the midnight of the local time (PST). (B) The normalized number concentration. The normalized plot is derived by dividing each observation (consisting of approximately 150 points between 20 and 600 nm) by the highest concentration in each measurement.

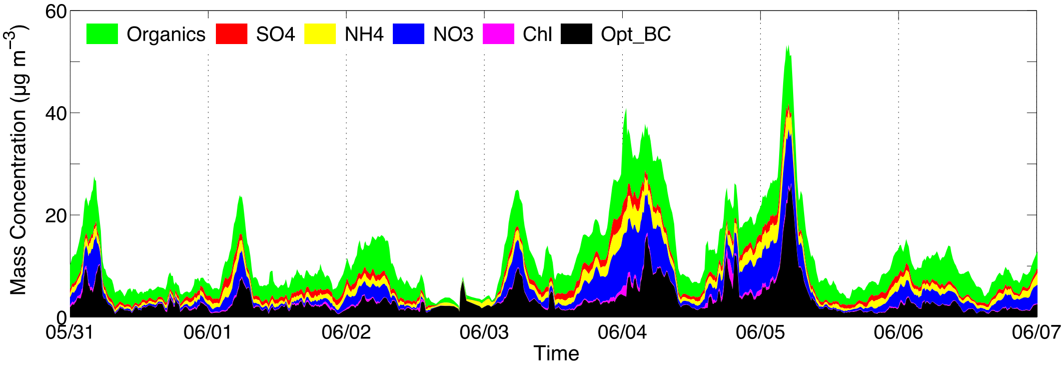

Fig. 3. The ACSM mass concentrations of ammonium (yellow), sulfate (red), organic (green), nitrate (blue), and chloride (purple) and the optically derived BC concentration (Opt_BC). The summation of the mass concentrations of the various constituents provides the equivalent $PM_{1.0}$ mass concentration (μg m^{-3}). The dates marked correspond to the midnight of the local time. (For interpretation of the references to color in this figure legend, the reader is referred to the web version of this article.)

concentration is also derived on the basis of the volatility measurements, with an average Vol_BC concentration of 3.22 ± 2.33 μg m^{-3}. The two BC concentrations determined by the two methodologies are compared in Fig. 4A, showing a good agreement with respect to the temporal trend and magnitude and with a correlation coefficient of 0.73. A scatterplot of the comparison is provided in Fig. 4B. Overnight, the Vol_BC concentration may be slightly biased to a higher value due to increased charring when aerosols are more heavily coated.

In Fig. 5, the $PM_{1.0}$ concentration (μg m^{-3}) determined by the summation of the ACSM measured mass loadings and the Opt_Bc concentrations is shown along with the $PM_{0.6}$ concentration, which is calculated from the measured number size distributions and size-resolved effective densities using Equation (4). The average mass concentration derived from APM measurements ($PM_{0.6}$) and ACSM measurements ($PM_{1.0}$) is 10.39 ± 7.61 μg m^{-3} and 13.04 ± 7.94 μg m^{-3}, respectively. The two data sets exhibit a similar temporal trend and concentration. These measurements are comparable with the previously reported $PM_{2.5}$ concentration of 16.00 ± 3.50 μg m^{-3} (Mota-Raigoza, 2012) in this region. Over the average day, the peak mass concentrations occur near 8 am (27.57 μg m^{-3}), and the lowest value is observed at 6 pm (7.41 μg m^{-3}). The highest 24 h mass concentration measured throughout the field campaign is 16.70 μg m^{-3} observed on 05 June. The BC percentage in the $PM_{1.0}$ concentration is plotted in Fig. 5 to depict the relative contribution of BC to $PM_{1.0}$. Overall, the BC concentration accounts for a greater percentage during the daytime. A strong correlation (with a correlation coefficient of 0.84) between the Opt_BC concentration and $PM_{0.6}$ is observed (Fig. 4C), indicating that BC emissions strongly influence the overall $PM_{0.6}$ population. Occasionally, the BC concentration alone exceeds the annual US EPA standard of $PM_{2.5}$ of 12 μg m^{-3}. The current US standard for $PM_{2.5}$ is 35 μg m^{-3} for a 24 h period, and the annual average $PM_{2.5}$ standard is 12 μg m^{-3}. There currently does not exist a $PM_{2.5}$ standard prescribed by SEMARNAT.

Table 2
Summary of aerosol properties by particle size for Cal–Mex 2010 in Tijuana, Mexico.

Particle size	Effective density (g cm^{-3})	Mode 1	Mode 2	Average HGF	Mode 1	Mode 2
46 nm	1.32 ± 0.11	–	1.3	1.09 ± 0.04	1.06	–
81 nm	1.31 ± 0.10	–	1.17	1.09 ± 0.05	1.02	–
151 nm	1.21 ± 0.13	0.64	1.44	1.16 ± 0.10	1	1.26
240 nm	1.27 ± 0.15	0.5	1.44	1.27 ± 0.17	1	1.36

Particle size	Average VGF	Mode 1	Mode 2	Concentration (cm^{-3})
46 nm	0.73 ± 0.03	0.51	0.99	13,500 ± 7560
81 nm	0.66 ± 0.04	0.41	0.95	7280 ± 4805
151 nm	0.62 ± 0.04	0.38	0.93	3.560 ± 2634
240 nm	0.56 ± 0.03	0.3	0.93	1.730 ± 1021

3.4. *Particle effective density*

Several previous studies have focused on the measurement of the effective density of ambient aerosols (McMurry et al., 2002; Geller et al., 2006; Malloy et al., 2009; Levy et al., 2013). In our present work, the effective density distribution is measured for four particle sizes (46, 81, 151, 240 nm), as shown in Fig. 6. The measurements are conducted approximately one to two hours apart, which allows for examination of the temporal trends and diurnal cycle in the effective density. For each effective density distribution, the weighted average effective density is calculated. The campaign-averaged effective density distributions are shown in Fig. 7. Inferences about the aerosol composition can be made from the average effective density and effective density distributions. Particles with an average effective density of near 1.77 g cm^{-3} are likely to be composed of ammonium sulfate (Qiu and Zhang, 2012), and an effective density between 1.00 and 1.40 g cm^{-3} (Turpin and Lim, 2001) can be attributed to organic aerosols. An effective density below 1.00 g cm^{-3} indicates the presence of fresh or slightly aged BC. In Fig. 8, the effective density distributions averaged during the afternoon (1–4 pm) and nights (1–4 am) during the campaign are plotted by the particle size.

Fig. 6A shows that the 46 nm particles have the most distinct and consistent diurnal cycle, and the average effective density is 1.32 ± 0.11 g cm^{-3}. The effective density distributions of 46 nm particles are unimodal, signifying a uniform or internally mixed aerosol composition. The lowest average effective densities (~0.90 g cm^{-3}) are observed during the afternoon hours (1–4 pm), and the highest average effective densities (~1.70 g cm^{-3}) are observed in the early morning (1–4 am) before the traffic. The lower effective density during the day likely corresponds with fresh BC associated with vehicle emissions. The increased effective density overnight may indicate the presence of emissions of primary organic aerosols or aged primary particles coated with organic aerosols. During the night, particles associated with fresh BC (<1.00 g cm^{-3}) account for less than 10% (Figs. 6A and 8A); however, during the day, this low-density mode accounts for a greater percentage, indicating a higher concentration of fresh BC during the day. Particles of 81 nm size, shown in Fig. 6B, exhibit a comparable diurnal cycle (ranging from 0.80 to 1.60 g cm^{-3}) to that of the 46 nm particles, and the average effective density (1.31 ± 0.10 g cm^{-3}) is also similar. The effective density

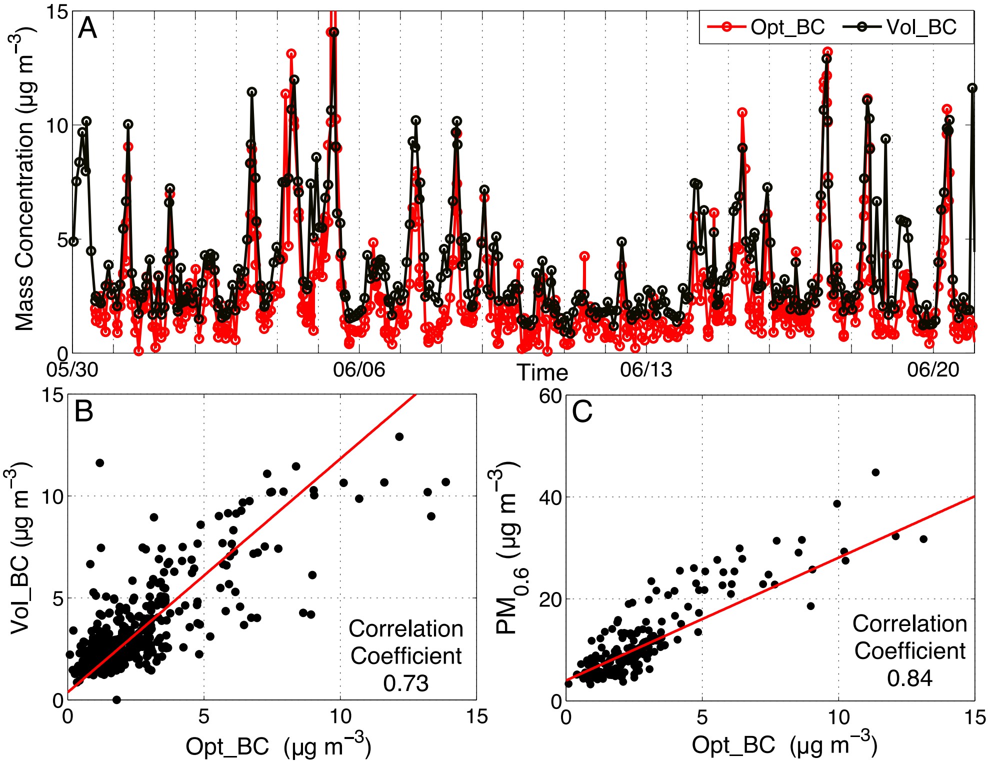

Fig. 4. (A) BC concentrations (μg m^{-3}) derived from two methodologies: from the volatility (Vol_BC, in black) and optical (Opt_BC, in red) measurements. The dates marked correspond to the midnight of the local time (PST). (B) Scatterplot of the BC contents derived from the two approaches. (C) A scatterplot of PM$_{0.6}$ and Opt_BC. (For interpretation of the references to color in this figure legend, the reader is referred to the web version of this article.)

distributions of 81 nm particles are unimodal (Fig. 7), also suggesting a uniform or internally mixed aerosol composition. The difference between night and day averaged effective density distributions of 81 nm particles (Fig. 8B) is less distinct compared to that of the 46 nm aerosols (Fig. 8A), but greater concentrations of BC are also observed in the daytime for 81 nm particles.

Particles of 151 and 240 nm clearly exhibit different effective density characteristics from the smaller particles. The average effective densities for 151 and 240 nm aerosols are 1.21 ± 0.13 g cm^{-3} and 1.27 ± 0.15 g cm^{-3}, respectively. The effective density distributions are typically bimodal, indicating an externally mixed aerosol population (Fig. 7). The effective density distributions of 151 and 240 nm particles (Fig. 6C and D) show a dominant (persistent) effective density mode near 1.50–1.60 g cm^{-3} and another secondary (less frequent) mode around 0.50 g cm^{-3}. Volatile organic compounds, formed from anthropogenic and biogenic sources, undergo photochemical oxidation to form oxidized products (Lei et al., 2000; McGivern et al., 2000; Lei and Zhang, 2001; Zhao et al., 2005a), some of which may be partitioned into the aerosol-phase (Zhao et al., 2005b; Qiu et al., 2011) to contribute to formation of secondary organic aerosols. Given the low biogenic contribution in this region (Zheng et al., 2013a, b), the more prominent mode in these distributions may be attributed to vehicle and industrial organic emissions and the secondary mode to BC. In addition, it has been suggested that the origin of much of organic aerosols observed in Tijuana (as much as 60% of organic

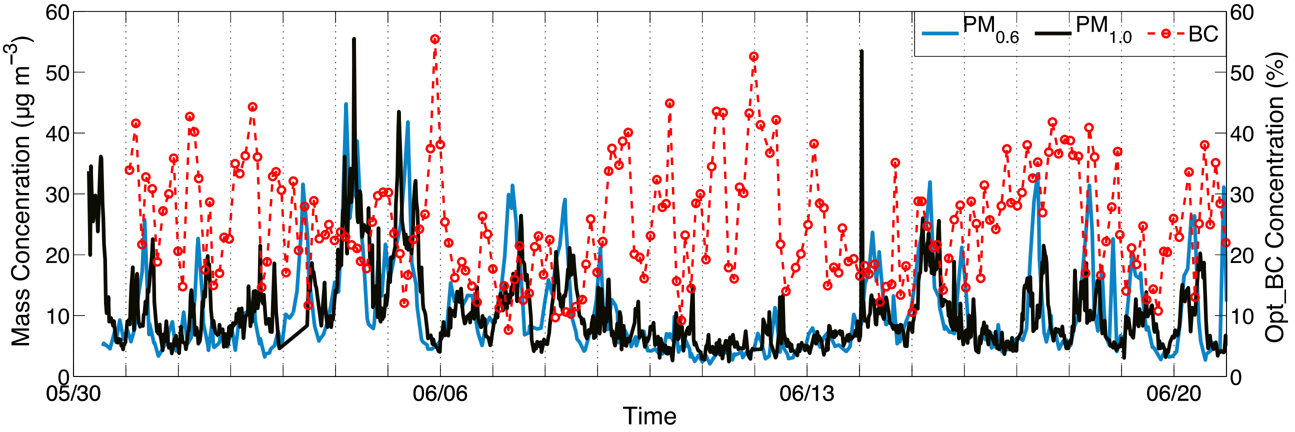

Fig. 5. Mass concentrations of PM$_{0.6}$ and PM$_{1.0}$ (μg m^{-3}) for the entire field campaign. The blue line indicates the calculated total mass concentration for 20–600 nm particles calculated using the number concentration and particle effective density. The black line denotes the PM$_{1.0}$ concentration determined by the summation of ACSM aerosol mass concentration and the optically derived BC concentration. The red dotted line designates the BC percentage of the PM$_{0.6}$ concentration. The dates marked correspond to the midnight of the local time. (For interpretation of the references to color in this figure legend, the reader is referred to the web version of this article.)

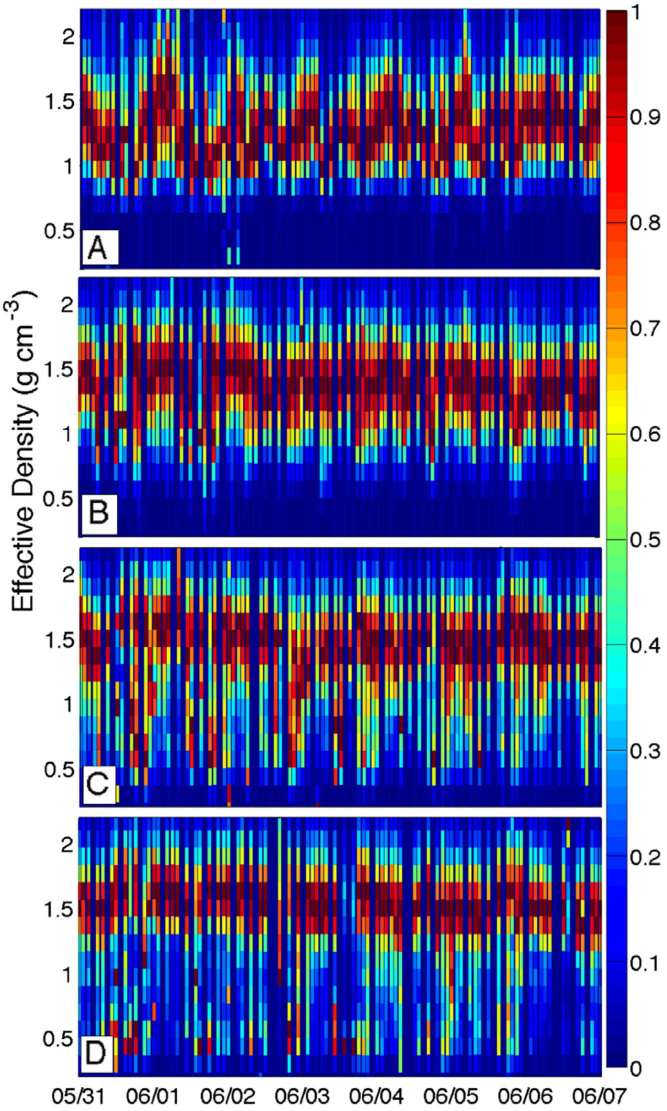

Fig. 6. Normalized particle effective density distributions for (A) 46 nm, (B) 81 nm, (C) 151 nm, and (D) 240 nm particles between 31 May and 07 June. The dates marked correspond to the midnight of the local time.

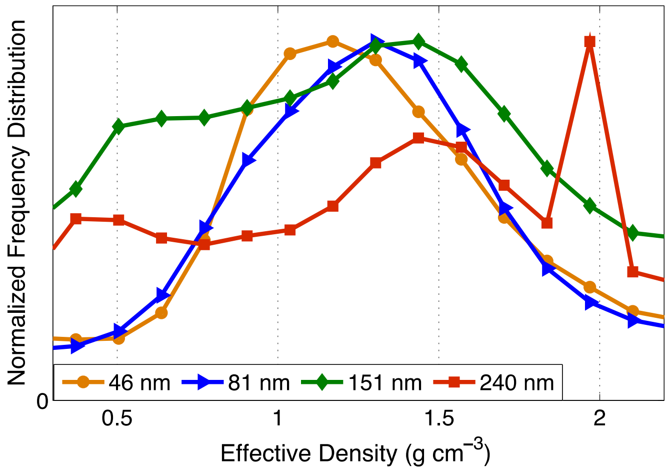

Fig. 7. The campaign-average aerosol effective density distributions for 46, 81, 151, and 240 nm particles during the entire field campaign.

matter) may be the Southern California Air Basin, because of long-range transport (Takahama et al., 2013). The effective density distribution of 240 nm particles demonstrate a third peak near 2.00 g cm^{-3} (Fig. 7), likely representing aged sea salt particles since most of the air masses originated over the Pacific Ocean (Fig. 1) and as also indicated by the presence of chloride in the ACSM composition measurements (Fig. 3). The secondary mode is most frequently observed in the afternoon (Fig. 8C and D). During the afternoon, about 40% and 30% of the effective density distributions are below 1.00 g cm^{-3} for the 151 and 240 nm aerosols, respectively, indicating a high concentration of BC. Overnight, an appreciably increased effective density is observed, and the effective density distributions become unimodal (Fig. 8C and D), indicating a change in the particle mixing state. These large particles at night likely correspond to an internal mixture of BC and organic aerosols. The average particle effective densities obtained are also summarized in Table 2.

3.5. *Aerosol optical properties*

The combined CRDS and nephelometer measurements provide the time series of aerosol extinction, scattering, and absorption coefficients (Fig. 9A) as well the SSA (Fig. 9B). In Fig. 10, the optical measurements are hourly averaged to illustrate the temporal trend. The average extinction, scattering, and absorption coefficients are 86.04, 63.07, and 22.97 Mm^{-1}, respectively. Over the course of a day, the average extinction coefficient ranges between 161.02 and 47.80 Mm^{-1}, as shown in Fig. 10. This is lower than measurements from Mexico City (Paredes-Miranda et al., 2009), but higher than observations from Houston, Texas (Levy et al., 2013). The highest scattering and absorption coefficients occur in the morning (6–10 am), and the lowest coefficients are observed near sunset. Since the planetary boundary layer (PBL) expands during the daytime, leading to aerosol dilution in the vertical direction, this likely explains the decreases in the total aerosol number concentration and extinction in the afternoon hours. There is a slight increase in light attenuation after sunset, likely due to the decrease in the PBL height. During the weekdays (i.e., 31 May–04 June), the highest scattering coefficients rarely exceed 150 Mm^{-1}. However, on Friday (04 June) and Saturday (05 June), there is an overall increase in scattering (exceeding 250 Mm^{-1}) and absorption (exceeding 100 Mm^{-1}), likely due to an increase of the traffic. There is also a distinct increase in the early morning (1–4 am) on Saturday correlated with the increased aerosol number concentration. The scattering and absorption coefficients are lower on Sunday (06 June), and there is not a distinct midmorning peak.

The average SSA is 0.75 and ranges from 0.71 to 0.78 on a daily base (Fig. 10), indicating a significant concentration of absorptive aerosols. On several occasions, a value of SSA below 0.50 is measured, which can be attributed to fresh emissions from diesel vehicles (Sheridan et al., 2005). The SSA value measured in our study is much lower than those in many highly populated US cities, such as Atlanta, Georgia (0.87 ± 0.08) in 1999 (Carrico et al., 2003) and Houston, TX (0.94 ± 0.04) in 2009 (Levy et al., 2013), but is comparable to Mexico City, which ranges between 0.60 and 0.85 (Paredes-Miranda et al., 2009). There are two distinct minima in the SSA diurnal trend. The lowest minimum is observed in the morning (7–8 am), and the secondary minimum occurs in the evening (7–9 pm). Although the magnitude of both scattering and absorption coefficients increases notably on Friday and Saturday, there is not a prominent change in the single scattering albedo. Only less than 1% of the SSA measurements have a value of greater than 0.95; this is in contrast to our optical measurements in Houston, TX, where much higher SSA values have been observed due to the higher organic and sulfate concentrations (Levy et al., 2013).

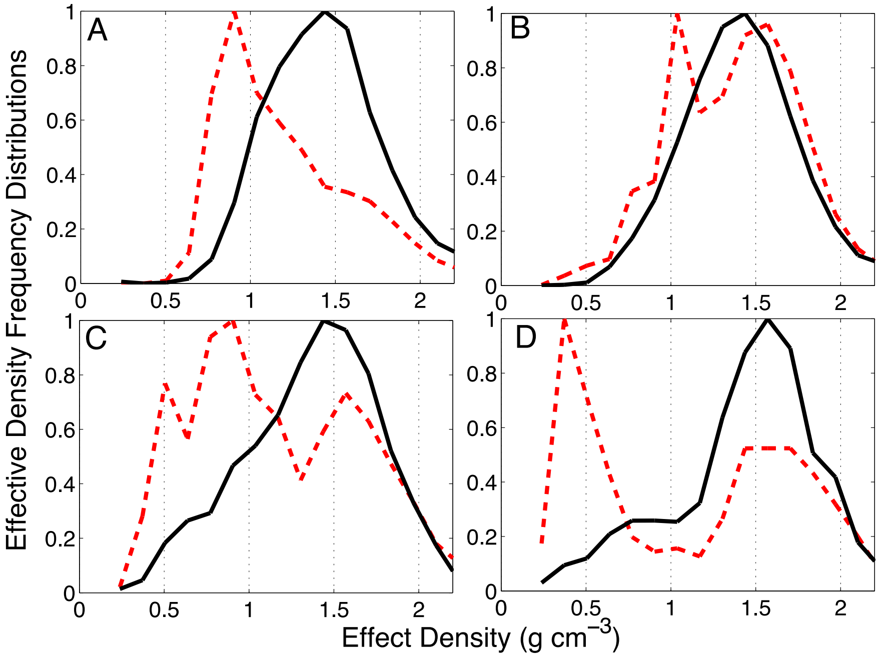

Fig. 8. Average aerosol effective density distributions for 46, 81, 151, and 240 nm particles during daytime (red dashed) and nighttime (black). (For interpretation of the references to color in this figure legend, the reader is referred to the web version of this article.)

3.6. Aerosol hygroscopicity

From the HV–TDMA measurements, HGFs for four particle sizes of 46, 81, 151, and 240 nm are obtained. Approximately, five HGF distributions, consisting of 45 points with the HGF values between 0.80 and 2.20, are obtained between 8 am and 6 pm on a daily basis. The weighted average HGFs of each distribution are shown in Fig. 11, and the campaign-average HGF distributions are depicted in Fig. 12. An HGF of unity indicates no modification to the particle size after exposure to 90% relative humidity, and a value greater than one indicates an increase in size. Pure ammonium sulfate exhibits an HGF near 1.70 at 90% RH (Wise et al., 2003). Freshly emitted BC particles are initially hydrophobic and exhibit HGFs near unity (Khalizov et al., 2009b; Khalizov et al., 2012). Aged BC particles may restructure upon humidification, resulting in a HGF below unity, which is observed in the particles greater than 100 nm (Khalizov et al., 2009b). Organic aerosols exhibit HGFs ranging from 1.08 to 1.17 at 90% RH dependent on the composition (Varutbangkul et al., 2006; Gysel et al., 2007; Meier et al., 2009). It is evident from Fig. 11

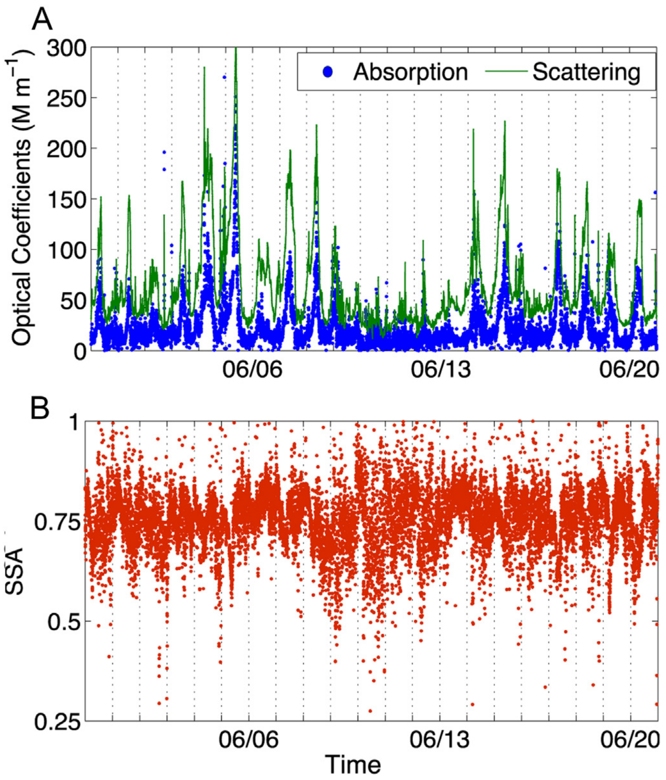

Fig. 9. Optical properties of aerosols observed during the field campaign. (A) Measured scattering (green) and absorption (blue) coefficients (Mm^{-1}) (B) Single scattering albedo. The dates marked correspond to the midnight of the local time. (For interpretation of the references to color in this figure legend, the reader is referred to the web version of this article.)

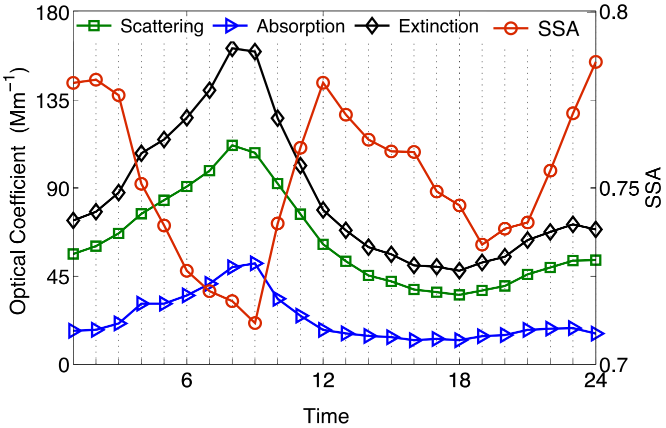

Fig. 10. Average diurnal cycle of the aerosol optical properties from the observational period. Extinction (black), scattering (green), and absorption (blue) are plotted on the left axis in Mm^{-1}, and SSA is plotted on the right axis. (For interpretation of the references to color in this figure legend, the reader is referred to the web version of this article.)

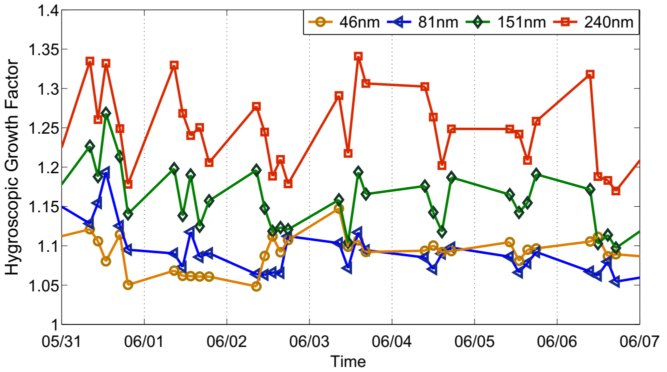

Fig. 11. Average aerosol hygroscopic growth factors (HGFs) measured between 31 May and 07 June for the four particle sizes. The dates marked correspond to the midnight of the local time.

that larger particles are more hygroscopic than smaller particles. For the four particles sizes of 46, 81, 151, and 240 nm, the average HGFs are 1.09 ± 0.40, 1.09 ± 0.05, 1.16 ± 0.10, and 1.27 ± 0.17, respectively. The hygroscopicity measurements indicate that the HGF distributions of 46 and 81 nm particles are dominantly unimodal, consistent with the effective density measurements. Both particle sizes exhibit a dominant hygroscopic mode between 1.00 and 1.10 and a small percentage in the HGF distribution above 1.20 (less than 1% and about 2%, respectively). The measured HGFs indicate that smaller particles are largely composed of non-hygroscopic materials, such as primary organic aerosols or BC. The HGF distributions of 151 nm particles are frequently bimodal throughout the field campaign, with the peaks near 1.30 and 1.00. The largest particles of 240 nm show also a bimodal hygroscopic distribution with the major peak occurring near 1.40 and the secondary peak near 1.00 (Fig. 12) and have the highest average HGF (Fig. 11). The HGF values of both 151 and 240 nm particles indicate that these larger particles correspond to an external mixture of fresh BC and secondary organic aerosols. Both 151 and 240 nm particles exhibit HGFs below 1.00 (31% and 25% in the HGF distribution, respectively), indicating restructured BC (Khalizov et al., 2009b). The hygroscopicity measurements also indicate a low concentration of ammonium sulfate, since little hygroscopicity distribution exhibits HGF > 1.60 (Wise et al., 2003). Note that during the observational period the HGF measurements are too sporadic to resolve a clear temporal trend. The average HGFs obtained are also summarized in Table 2.

3.7. *Aerosol volatility*

In the aerosol volatility measurements, aerosols are heated to a temperature near 350 °C, and the remaining mass reflects non-volatile materials, such as elemental carbon. The HV–TDMA measurements contain 45 points with the VGF values between 0.30 and 1.20 for each VGF distribution. Note that a decreasing VGF indicates increasing volatility, and a value of unity would indicate that all of the concentration persisted after heat exposure. The weighted-average VGFs from each distribution are shown in Fig. 13, and the campaign-averaged VGF distributions are provided in Fig. 14. Similar to that of the hygroscopicity measurements, there is a clear dependence of the particle volatility on particle size (Fig. 13): smaller particles are less volatile than larger particles. All particle sizes exhibit a distinct peak between 0.80 and 1.20 in the volatility distribution, indicating a significant presence of non-volatile matter such as BC (Fig. 14). There is also a secondary peak below 0.60 in all particle sizes. As the particles increase in diameter, the secondary peak becomes more volatile, most likely due to an increased organic fraction (Salo et al., 2011). Particles of 46 nm have the highest average VGF (0.73 ± 0.03), ranging between 0.60 and 0.90 (Fig. 13) throughout the field campaign. The average VGF distribution of 46 nm particles has one major peak near 1.00 and a broad region of increased VGF between 0.50 and 0.85 (Fig. 14). For 81 nm particles, the average VGF is 0.66 ± 0.04, ranging between 0.55 and 0.76, and the two VGF modes occur at 0.41 and 0.95. For the 151 nm and 240 nm particles, the average VGFs are 0.62 ± 0.04 and 0.56 ± 0.03, respectively. The bimodal peaks occur at 0.38 and 0.93 for 151 nm particles and at 0.30 and 0.93 for 240 nm particles. Interestingly, the highest peak of the non-volatile material (VGF between 0.80 and 1.20) is observed for 151 nm particles, consistent with the lowest effective density observed in this size (Table 2) and the highest peak in the low-density mode (about 0.5 g cm^{-3}). This is explained by the fact that the frequency of the presence of BC is the highest for this particle size averaged over the entire campaign period. The 240 nm particles have the most volatile secondary peak (Fig. 14), which is also consistent with the largest HGF for this particle size (Fig. 12). Diurnally, VGFs are lower at night for the 151 and 240 nm particles and higher during the day (Fig. 13), reflecting a larger organic fraction during the night, since aged BC with

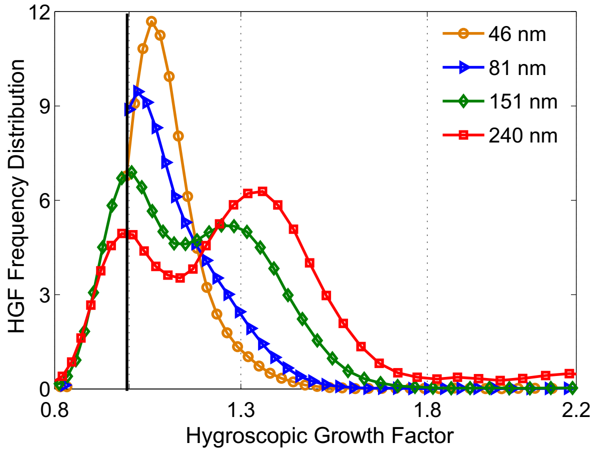

Fig. 12. The campaign-average aerosol hygroscopicity growth factor (HGF) distributions for 46, 81, 151, and 240 nm particles. The solid vertical line indicates an HGF of unity.

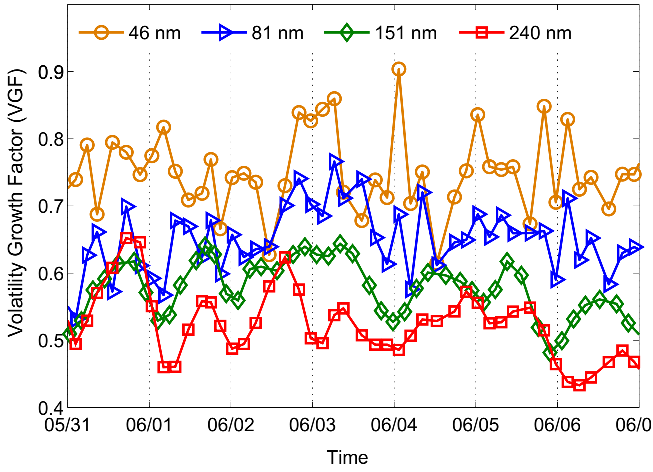

Fig. 13. Average aerosol volatility growth factors (VGF) measured between 31 May and 07 June for the four particle sizes. The dates marked correspond to the midnight of the local time.

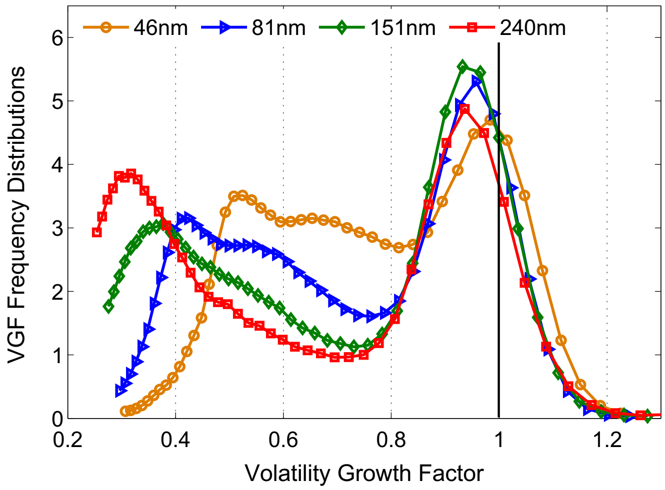

Fig. 14. The campaign-averaged aerosol volatility growth factor (VGF) distributions for 46, 81, 151, and 240 nm particles. The solid vertical line indicates a VGF of unity.

increased organic coating is more volatile. This VGF diurnal behavior is consistent with the higher effective density at night and the lower effective density in the afternoon. Hence, VGFs decrease with increasing mobility diameter, indicating a greater amount of volatile materials. This is also consistent with the observed increasing hygroscopicity with particle size. The average VGFs obtained are also summarized in Table 2.

4. Conclusions

The Cal–Mex 2010 field campaign was conducted to obtain concentrations of gaseous and PM pollutants that may be used by policymakers in future air quality and climate decisions. A comprehensive set of properties of ambient submicron aerosols was measured in Tijuana, near the California–Mexico border during May and June 2010, including the chemical compositions, optical properties, and the particle size, effective density, hygroscopicity, and volatility for four distinct particle sizes.

The average number concentration is 26,300 ± 15,300 particles cm^{-3} during the entire campaign period. The average mass concentration of $PM_{0.6}$ is calculated to be 10.39 ± 7.61 $\mu g\ m^{-3}$, ranging between 6 and 20 $\mu g\ m^{-3}$ on a daily basis. Typically, the aerosol concentration rises sharply near sunrise, remains elevated throughout the day, and decreases overnight. The highest aerosols concentrations are observed between 20 and 75 nm. There is little new particle formation or particle growth during the day in this region.

Measurements made by ACSM and the calculated BC content show that the mass loading is dominated by organic aerosols (37%) and BC (27%), along with small amount of nitrate, ammonia, and sea salt. The BC content is derived using two independent approaches on the basis of optical properties and volatility measurements, with the average BC concentrations of 2.87 ± 2.65 $\mu g\ m^{-3}$ and 3.22 ± 2.33 $\mu g\ m^{-3}$, respectively. The BC content in this US–Mexico border region is much higher than most of US urban cities, but comparable to that previously reported in other Mexican Cities (Yu et al., 2009; Hernández-Mena et al., 2011; Levy et al., 2013).

For four particle sizes of 46, 81, 151, and 240 nm, the particle effective density, HGFs, and VGFs are measured. For smaller particles of 46 and 81 nm, the effective density distribution is unimodal during the day and night, signifying a uniform or internally mixed aerosol composition. Also, the smaller particles show a noticeable diurnal trend in the effective density distribution, with the highest effective density (1.70 g cm^{-3}) occurring shortly after midnight and the lowest value (0.90 g cm^{-3}) occurring during the afternoon. In contrast, larger particles of 151 and 240 nm exhibit a bi-modal effective density distribution during the daytime, indicating an external mixture of fresh BC and organic aerosols, but a unimodal distribution during the night, corresponding to an internal mixture of BC and organic aerosols, which is characteristic of aged BC.

Both HGFs and VGFs measured are strongly size-dependent. HGFs increase with increasing particle size, indicating that the largest particles are more hygroscopic. On the other hand, VGFs decrease with increasing particle size, indicating that small particles are more non-volatile. The hygroscopicity distribution of smaller particles (46 and 81 nm) is unimodal, with a HGF value of close to unity. Large particles typically exhibit a bi-modal distribution, with a non-hygroscopic mode (i.e., a HGF value of close to unity) and another hygroscopic mode (with the HGF value of 1.3 and 1.4 for 151 and 240 nm particles, respectively). For all particle sizes, the VGF distributions are bimodal, with a primary non-volatile mode and secondary volatile mode. The secondary VGFs decrease with increasing particle size. The hygroscopicity measurements also reveal that smaller particles are largely internally mixed, while large particles are externally mixed. Hence, the HGF and VGF measurements can both be explained by the particle mixing state, which is also consistent with the effective density measurements.

The average extinction, scattering, and absorption coefficients in Tijuana are 86.04, 63.07, and 22.97 Mm^{-1}, respectively. The highest daytime extinction coefficients are observed in the midmorning hours, concurrent with the increase of BC and total mass concentration ($PM_{0.6}$). The average SSA is 0.75, which is much lower than those observed in many large US cities, also indicating a significant concentration of absorptive aerosols. Our working progress includes modeling of PM formation and transformation in this region using chemical transport models, to be reported separately.

In summary, our results reveal that gasoline and diesel vehicles produce a significant amount of BC particles in this US–Mexico border region, which impacts the regional environment and climate.

Acknowledgments

This work was supported by the National Science Foundation (AGS-1009727, AGS-1009408, and AGS-1009393) and the Robert A. Welch Foundation (A-1417). We acknowledged Alejandro Torres-Jaramillo and José Santos García-Yee for their support with the CCA-UNAM air quality mobile monitoring station during the campaign. S.T. and L.M.R acknowledged W. Richard Leaitch and Desi Toom-Sauntry for their support of the ACSM measurements. L.T.M. thanked support from the California Air Resources Board (09-356) and the Mexican National Institute of Ecology. G. Li acknowledged support from MIT Molina Fellowship.

References

Aiken, A.C., et al., 2010. Mexico City aerosol analysis during MILAGRO using high resolution aerosol mass spectrometry at the urban supersite (T0) – Part 2: Analysis of the biomass burning contribution and the modern carbon fraction. Atmos. Chem. Phys. 10, 5315–5341.

Anderson, T.L., Ogren, J.A., 1998. Determining aerosol radiative properties using the TSI 3563 integrating nephelometer. Aerosol Sci. Technol. 29 (1), 57–69. http://dx.doi.org/10.1080/02786829808965555.

Ban-Weiss, G.A., Lunden, M.M., Kirchstetter, T.W., Harley, R.A., 2010. Size-resolved particle number and volume emission factors for on-road gasoline and diesel motor vehicles. J. Aerosol Sci. 41 (1), 5–12. http://dx.doi.org/10.1016/j.jaerosci.2009.08.001.

Bei, N., Li, G., Zavala, M., Barrera, H., Torres, R., Grutter, M., Gutiérrez, W., García, M., Ruiz-Suarez, L.G., Ortinez, A., Guitierrez, Y., Alvarado, C., Flores, I., Molina, L.T., 2013. Meteorological overview and plume transport patterns during Cal-Mex 2010. Atmos. Environ 70, 477–489. http://dx.doi.org/10.1016/J.Atmosenv.2012.01.065.

Bei, N., Li, G., Zavala, M., Barrera, H., Torres, R., Grutter, M., Gutiérrez, W., García, M., Ruiz-Suarez, L.G., Ortinez, A., Guitierrez, Y., Alvarado, C., Flores, I., Molina, L.T., 2013.

Meteorological overview and plume transport patterns during Cal-Mex 2010. Atmos. Environ. 70, 477–489. http://dx.doi.org/10.1016/J.Atmosenv.2012.01.065.

Bond, T.C., Bergstrom, R.W., 2006. Light absorption by carbonaceous particles: an investigative review. Aerosol Sci. Technol. 40 (1), 27–67. http://dx.doi.org/10.1080/02786820500421521.

Bond, D.W., Steiger, S., Zhang, R., Tie, X., Orville, R.E., 2002. The importance of NO$_x$ production by lightning in the tropics. Atmos. Environ. 36, 1509–1519.

Border 2012, United States Environmental Protection Agency, and Secretaría de Medio Ambiente y Recursos Naturales, 2005. Border 2012: US-Mexico Environmental Program Overview Sheet. Web PDF File retrieved Oct 3, 2012 http://www.semarnat.gob.mx/temas/internacional/frontera2012/Paginas/Publicaciones.aspx.

Border 2012, United States Environmental Protection Agency, Secretaría de Medio Ambiente y Recursos Naturales, 2011. Border 2012: U.S.-Mexico Environmental Program, State of the Border Region Indicators Report 2010. Web PDF File retrieved Oct 3, 2012 http://www.epa.gov/border2012/indicators/docs/border-2012_indicator-rpt_eng.pdf.

Border 2020, United States Environmental Protection Agency, Secretaría de Medio Ambiente y Recursos Naturales, 2012. Border 2020 Factsheet. Border 2020: U.S.-Mexico Environmental Program Summary. Web PDF File retrieved Oct 3, 2012 http://www.epa.gov/border2020/pdf/border2020-factsheet.pdf.

Brinkhoff, T., 2012. City Population, Mexico: Major Cities. Web data retrieved August 2012 http://www.citypopulation.de/Mexico-Cities.html.

Carrico, C.M., Bergin, M.H., Xu, J., Baumann, K., Maring, H., 2003. Urban aerosol radiative properties: measurements during the 1999 Atlanta Supersite Experiment. J. Geophys. Res. Atmos. (1984–2012) 108 (D7). http://dx.doi.org/10.1029/2001JD001222.

Center of Information for Men and Women Workers, 2004. Mexican Maquiladora Status and Statistics. Web data retrieved November 2012 http://ueinternational.org/MLNA/mlna_articles.php?id=71.

Chow, J.C., Watson, J.G., Green, M.C., Lowenthal, D.H., Bates, B., Oslund, W., Torres, G., 2000. Cross-border transport and spatial variability of suspended particles in Mexicali and California's Imperial Valley. Atmos. Environ. 34 (11), 1833–1843. http://dx.doi.org/10.1016/S1352-2310(99)00282-4.

Croes, B.E., Fujita, E.M., 2003. Overview of the 1997 southern California ozone study (SCOS97-NARSTO). Atmos. Environ. 37, 3–26. http://dx.doi.org/10.1016/S1352-2310(03)00379-0.

Dominici, F., Peng, R.D., Bell, M.L., Pham, L., McDermott, A., Zeger, S.L., Samet, J.M., 2006. Fine particulate air pollution and hospital admission for cardiovascular and respiratory diseases. J. Am. Med. Assoc. 295 (10), 1127–1134. http://dx.doi.org/10.1001/jama.295.10.1127.

EPA/CICA, 1997–2007. Border Air Quality Data – Monitor Values Reports. Web data retrieved September 2012 http://www.epa.gov/ttn/catc/cica/geosel_e.html.

Fan, J., Zhang, R., Li, G., Tao, W.K., 2007. Effects of aerosols and relative humidity on cumulus clouds. J. Geophys. Res. Atmos. (1984–2012) 112 (D14, D14204). http://dx.doi.org/10.1029/2006JD008136.

Fan, J., Zhang, R., Tao, W.K., Mohr, K.I., 2008. Effects of aerosol optical properties on deep convective clouds and radiative forcing. J. Geophys. Res. Atmos. (1984–2012) 113 (D8, D08209). http://dx.doi.org/10.1029/2007JD009257.

Forster, P., Ramaswamy, V., Artaxo, P., Berntsen, T., Betts, R., Fahey, D.W., Haywood, J., Lean, J., Lowe, D.C., Myhre, G., Nganga, J., Prinn, R., Raga, G., Schulz, M., Van Dorland, R., 2007. Changes in atmospheric constituents and in radiative forcing. Climate Change 20.

Gasparini, R., Li, R., Collins, D.R., 2004. Integration of size distributions and size-resolved hygroscopicity measured during the Houston supersite for compositional categorization of the aerosol. Atmos. Environ. 38 (20), 3285–3303. http://dx.doi.org/10.1016/j.atmosenv.2004.03.019.

Geller, M., Biswas, S., Sioutas, C., 2006. Determination of particle effective density in urban environments with a differential mobility analyzer and aerosol particle mass analyzer. Aerosol Sci. Technol. 40 (9), 709–723. http://dx.doi.org/10.1080/02786820600803925.

Gysel, M., Crosier, J., Topping, D.O., Whitehead, J.D., Bower, K.N., Cubison, M.J., Williams, P.I., Flynn, M.J., McFiggans, G.B., Coe, H., 2007. Closure study between chemical composition and hygroscopic growth of aerosol particles during TORCH2. Atmos. Chem. Phys. 7 (24), 6131–6144.

Haywood, J., Boucher, O., 2000. Estimates of the direct and indirect radiative forcing due to tropospheric aerosols: a review. Rev. Geophys. 38 (4), 513–543. http://dx.doi.org/10.1029/1999RG000078.

Hernández-Mena, L., Saldarriaga-Noreña, H., Murillo-Tovar, M.A., Amador-Muñoz, O., López-López, A., Waliszewski, S.M., 2011. Determination of black carbon in fine particles using a semi-continuous method at two sites in the city of Guadalajara, Mexico, during 2007. Bull. Environ. Contam. Toxicol. 87 (3), 336–342. http://dx.doi.org/10.1007/s00128-011-0330-z.

Kelly, K., Wagner, D., Lighty, J., Núñez, M.Q., Vazquez, F.A., Collins, K., Barud-Zubillaga, A., 2006. Black carbon and polycyclic aromatic hydrocarbon emissions from vehicles in the United States–Mexico border region: pilot study. J. Air Waste Manag. Assoc. 56 (3), 285–293. http://dx.doi.org/10.1080/10473289.2006.10464465.

Khalizov, A.F., Hogan, B., Qiu, C., Petersen, E.L., Zhang, R., 2012. Characterization of soot aerosol produced from combustion of propane in a shock tube. Aerosol Sci. Technol. 46, 925–936.

Khalizov, A.F., Lin, Y., Qiu, C., Guo, S., Collins, D., Zhang, R., 2013. The role of OH-initiated oxidation of isoprene in aging of combustion soot. Environ. Sci. Technol. 47, 2254–2263. http://dx.doi.org/10.1021/es3045339.

Khalizov, A.F., Xue, H., Wang, L., Zheng, J., Zhang, R., 2009a. Enhanced light absorption and scattering by carbon soot aerosol internally mixed with sulfuric acid. J. Phys. Chem. A 113 (6), 1066–1074. http://dx.doi.org/10.1021/jp807531n.

Khalizov, A.F., Zhang, R., Zhang, D., Xue, H., Pagels, J., McMurry, P.H., 2009b. Formation of highly hygroscopic soot aerosols upon internal mixing with sulfuric acid vapor. J. Geophys. Res. Atmos. (1984–2012) 114 (D5, D05208). http://dx.doi.org/10.1029/2008JD010595.

Lange, J.E., Lauer, E., Voas, R.B., 1999. A survey of the San Diego–Tijuana cross-border binging: methods and analysis. Eval. Rev. 23 (4), 378–398. http://dx.doi.org/10.1177/0193841X9902300402.

Lei, W., Zhang, R., 2001. Theoretical study of hydroxy-isoprene alkoxy radicals and their decomposition pathways. J. Phys. Chem. 105, 3808–3815.

Lei, W., Zhang, R., McGivern, W.S., Derecskei-Kovacs, A., North, S.W., 2000. Theoretical study of isomeric branching in the isoprene-OH reaction: implications to final product yields in isoprene oxidation. Chem. Phys. Lett. 326, 109–114.

Levy, M.E., Zhang, R., Khalizov, A.F., Zheng, J., Collins, D.R., Glen, C.R., Wang, Y., Yu, X.-Y., Luke, W., Jayne, J.T., Olaguer, E., 2013. Measurements of submicron aerosols in Houston, Texas during the 2009 SHARP field campaign. J. Geophys. Res. Atmos. 118. http://dx.doi.org/10.1002/jgrd.50785.

Li, G., Zhang, R., Fan, J., Tie, X., 2005. Impacts of black carbon aerosol on photolysis and ozone. J. Geophys. Res. 110, D23206. http://dx.doi.org/10.1029/2005JD005898.

Malloy, Q.G., Nakao, S., Qi, L., Austin, R., Stothers, C., Hagino, H., Cocker III, D.R., 2009. Real-time aerosol density determination utilizing a modified scanning mobility particle sizer—Aerosol particle mass analyzer system. Aerosol Sci. Technol. 43 (7), 673–678. http://dx.doi.org/10.1080/02786820902832960.

Massoli, P., Bates, T.S., Quinn, P.K., Lack, D.A., Baynard, T., Lerner, B.M., Tucker, S.C., Brioude, J., Stohl, A., Williams, E.J., 2009. Aerosol optical and hygroscopic properties during TexAQS-GoMACCS 2006 and their impact on aerosol direct radiative forcing. J. Geophys. Res. Atmos. (1984–2012) 114 (D7). http://dx.doi.org/10.1029/2008JD011604.

McGivern, S., Suh, I., Clinkenbeard, A.D., Zhang, R., North, S.W., 2000. Experimental and computational study of the OH-isoprene reaction: Isomeric branching and low-pressure behavior. J. Phys. Chem. 104, 6609–6616.

McMurry, P.H., Wang, X., Park, K., Ehara, K., 2002. The relationship between mass and mobility for atmospheric particles: a new technique for measuring particle density. Aerosol Sci. Technol. 36 (2), 227–238. http://dx.doi.org/10.1080/027868202753504083.

Meier, J., Wehner, B., Massling, A., Birmili, W., Nowak, A., Gnauk, T., Brüggemann, E., Herrmann, H., Min, H., Wiedensohler, A., 2009. Hygroscopic growth of urban aerosol particles in Beijing (China) during wintertime: a comparison of three experimental methods. Atmos. Chem. Phys. 9 (18), 6865–6880. http://dx.doi.org/10.5194/acp-9-6865-2009.

Mendoza, A., Pardo, E.I., Gutierrez, A.A., 2010. Chemical characterization and preliminary source contribution of fine particulate matter in the Mexicali/Imperial Valley border area. J. Air Waste Manag. Assoc. 60 (3), 258–270. http://dx.doi.org/10.3155/1047-3289.60.3.258.

Mokdad, A.H., Marks, J.S., Stroup, D.F., Gerberding, J.L., 2004. Actual causes of death in the United States, 2000. J. Am. Med. Assoc. 291 (10), 1238–1245. http://dx.doi.org/10.1001/jama.291.10.1238.

Molina, M.J., Molina, L.T., Zhang, R., Meads, R., Spencer, D., 1997. Heterogeneous reaction of ClONO$_2$ with HCl on aluminum oxide. Geophys. Res. Lett. 24, 1619–1622.

Mota-Raigoza, A., 2012. Characterization of Traffic Related Air Pollution Particulate Matter Mass and Surface Area Concentrations in the Border Community of San Ysidro and the Tijuana River National Estuarine. San Diego State University, San Diego, CA. http://hdl.handle.net/10211.10/2609.

Nesbitt, S.W., Zhang, R., Orville, R.E., 2000. Seasonal and global NO$_x$ production by lightning estimated from the Optical Transient Detector (OTD). Tellus B 52, 1206–1215.

Ng, N.L., Herndon, S.C., Trimborn, A., Canagaratna, M.R., Croteau, P.L., Onasch, T.B., Sueper, D., Worsnop, D.R., Zhang, Q., Sun, Y.L., Jayne, J.T., 2011. An aerosol chemical speciation monitor (ACSM) for routine monitoring of the composition and mass concentrations of ambient aerosol. Aerosol Sci. Technol. 45 (7) pii: 934555189.

Pagels, J., McMurry, P.H., Khalizov, A.F., Zhang, R., 2009. Processing of soot by controlled sulphuric acid and water condensation—Mass and mobility relationship. Aerosol Sci. Technol. 43, 629–640.

Paredes-Miranda, G., Arnott, W.P., Jimenez, J.L., Aiken, A.C., Gaffney, J.S., Marley, A., 2009. Primary and secondary contributions to aerosol light scattering and absorption in Mexico City during the MILAGRO 2006 campaign. Atmos. Chem. Phys. 9, 3721–3730. http://dx.doi.org/10.5194/acp-9-3721-2009.

Qiu, C., Zhang, R., 2012. Physiochemical properties of alkylaminium sulfates: hygroscopicity, Thermostability, and density. Environ. Sci. Technol. 46 (8), 4474–4480. http://dx.doi.org/10.1021/es3004377.

Qiu, Q., Wang, L., Lal, V., Khalizov, A.F., Zhang, R., 2011. Heterogeneous chemistry of alkylamines on ammonium sulfate and ammonium bisulfate. Environ. Sci. Technol. 45, 4748–4755.

Radney, J.G., Bazargan, M.H., Wright, M.E., Atkinson, D.B., 2009. Laboratory validation of aerosol extinction coefficient measurements by a field-deployable pulsed cavity ring-down transmissometer. Aerosol Sci. Technol. 43 (1), 71–80. http://dx.doi.org/10.1080/02786820802482536.

Ramanathan, V., Crutzen, P.J., Kiehl, J.T., Rosenfeld, D., 2001. Atmosphere, aerosols, climate, and the hydrological cycle. Science 294 (5549), 2119–2124. http://dx.doi.org/10.1126/science.1064034.

Salo, K., Hallquist, M.M., Jonsson, Å.M., Saathoff, H., Naumann, K.-H., Spindler, C., Tillmann, R., Fuchs, H., Bohn, B., Rubach, F., Mentel, Th.F., Müller, L., Reinnig, M., Hoffmann, T., Donahue, N.M., 2011. Volatility of secondary organic aerosol during OH radical induced ageing. Atmos. Chem. Phys. 11, 11055–11067. http://dx.doi.org/10.5194/acp-11-11055-2011.

Sheridan, P.J., Arnott, W.P., Ogren, J.A., Andrews, E., Atkinson, D.B., Covert, D.S., Moosmüller, H., Petzold, A., Schmid, B., Strawa, A.W., Varma, R., Virkkula, A., 2005. The Reno aerosol optics study: an evaluation of aerosol absorption measurement methods. Aerosol Sci. Technol. 39 (1), 1–16. http://dx.doi.org/10.1080/027868290901891.

Shi, C., Fernando, H.J.S., Yang, J., 2009. Contributors to ozone episodes in three U.S./Mexico border twin-cities. Science of the Total Environment 407 (18), 5128–5138. http://dx.doi.org/10.1016/J.Scitotenv.2009.05.046.

Shores, C.A., Klapmeyer, M.E., Quadros, M.E., 2013. Sources and transport of black carbon at the California-Mexico border. Atmos. Environ. 70, 490–499. http://dx.doi.org/10.1016/J.Atmosenv.2012.04.031.

Smith, J.D., Atkinson, D.B., 2001. A portable pulsed cavity ring-down transmissometer for measurement of the optical extinction of the atmospheric aerosol. Analyst 126 (8), 1216–1220. http://dx.doi.org/10.1039/B101491I.

Sun, Y.L., Wang, Z.F., Fu, P.Q., Yang, T., Jiang, Q., Dong, H.B., Li, J., Jia, J.J., 2013. Aerosol composition, sources and processes during wintertime in Beijing, China. Atmos. Chem. Phys. Discuss. 13, 2077–2123. http://dx.doi.org/10.1039/B101491I.

Swietlicki, E., Hansson, H.-C., Hämeri, K., Svenningsson, B., Massling, A., Mcfiggans, G., Mcmurry, P.H., Petäjä, T., Tunved, P., Gysel, M., Topping, D., Weingartner, E., Baltensperger, U., Rissler, J., Wiedensohler, A., Kulmal, M., 2008. Hygroscopic properties of submicrometer atmospheric aerosol particles measured with H-TDMA instruments in various environments—a review. Tellus B 60 (3), 432–469. http://dx.doi.org/10.1111/j.1600-0889.2008.00350.x.

Takahama, S., Johnson, A., Guzman Morales, J., Russell, L.M., Duran, R., Rodriguez, G., Zheng, J., Zhang, R., Toom-Sauntry, D., Leaitch, W.R., 2013. Submicron organic aerosol in Tijuana, Mexico, from local and southern California sources during the CalMex campaign. Atmos. Environ. 70, 500–512. http://dx.doi.org/10.1016/j.atmosenv.2012.07.057.

Turpin, B.J., Lim, H.J., 2001. Species contributions to $PM_{2.5}$ mass concentrations: revisiting common assumptions for estimating organic mass. Aerosol Sci. Technol. 35 (1), 602–610. http://dx.doi.org/10.1080/02786820119445.

Varutbangkul, V., Brechtel, F.J., Bahreini, R., Ng, N.L., Keywood, M.D., Kroll, J.H., Flagan, R.C., Seinfeld, J.H., Lee, A., Goldstein, A.H., 2006. Hygroscopicity of secondary organic aerosols formed by oxidation of cycloalkenes, monoterpenes, sesquiterpenes, and related compounds. Atmos. Chem. Phys. 6 (9), 2367–2388.

Villani, P., Picard, D., Marchand, N., Laj, P., 2007. Design and validation of a 6–volatility tandem differential mobility analyzer (VTDMA). Aerosol Sci. Technol. 41 (10), 898–906. http://dx.doi.org/10.1080/02786820701534593.

Wang, H., Jacob, D.J., Le Sager, P., Streets, D.G., Park, R.J., Gilliland, A.B., Van Donkelaar, A., 2009. Surface ozone background in the United States: Canadian and Mexican pollution influences. Atmos. Environ. 43 (6), 1310–1319. http://dx.doi.org/10.1016/j.atmosenv.2008.11.036.

Wang, L., Khalizov, A.F., Zheng, J., Xu, W., Lal, V., Ma, Y., Zhang, R., 2010a. Atmospheric nanoparticles formed from heterogeneous reactions of organics. Nat. Geosci. 3, 238–242. http://dx.doi.org/10.1038/ngeo778.

Wang, L., Lal, V., Khalizov, A.F., Zhang, R., 2010b. Heterogeneous chemistry of alkylamines with sulfuric acid: implications for atmospheric formation of alkylaminium sulfates. Environ. Sci. Technol. 44, 2461–2465. http://dx.doi.org/10.1021/es9036868.

Wise, M.E., Surratt, J.D., Curtis, D.B., Shilling, J.E., Tolbert, M.A., 2003. Hygroscopic growth of ammonium sulfate/dicarboxylic acids. J. Geophys. Res. 108 (D20), 4638. http://dx.doi.org/10.1029/2003JD003775.

Xue, H., Khalizov, A.F., Wang, L., Zheng, J., Zhang, R., 2009a. Effects of dicarboxylic acid coating on the optical properties of soot. Phys. Chem. Chem. Phys. 11, 7865–7875. http://dx.doi.org/10.1039/b700001a.

Xue, H., Khalizov, A.F., Zhang, R., 2009b. Effects of coating of dicarboxylic acids on the mass-mobility relationship of soot particles. Environ. Sci. Technol. 43, 2787–2792.

Yu, X.Y., Cary, R.A., Laulainen, N.S., 2009. Primary and secondary organic carbon downwind of Mexico City. Atmos. Chem. Phys. 9, 6793–6814.

Yue, D.L., Hu, M., Zhang, R., Wang, Z.B., Zheng, J., Wu, Z.J., Wiedensohler, A., He, L.Y., Huang, X.F., Zhu, T., 2010. The roles of sulfuric acid in new particle formation and growth in the mega-city of Beijing. Atmos. Chem. Phys. 10, 4953–4960.

Zhang, R., 2010. Getting to the critical nucleus of aerosol formation. Science 328, 1366–1367. http://dx.doi.org/10.1126/science.1189732.

Zhang, R., Leu, M.T., Keyser, L.F., 1996a. Heterogeneous chemistry of HONO on liquid sulfuric acid: a new mechanism of chlorine activation on stratospheric sulfate aerosols. J. Phys. Chem. 100, 339–345.

Zhang, R., Leu, M.T., Molina, M.J., 1996b. Formation of polar stratospheric clouds on preactivated background aerosols. Geophys. Res. Lett. 23, 1669–1672.

Zhang, R., Lei, W., Tie, X., Hess, P., 2004a. Industrial emissions cause extreme diurnal urban ozone variability. Proc. Natl. Acad. Sci. U. S. A. 101, 6346–6350.

Zhang, R., Suh, I., Zhao, J., Zhang, D., Fortner, E.C., Tie, X., Molina, L.T., Molina, M.J., 2004b. Atmospheric new particle formation enhanced by organic acids. Science 304, 1487–1490.

Zhang, R., Li, G., Fan, J., Wu, D.L., Molina, M.J., 2007. Intensification of Pacific storm track linked to Asian pollution. Proc. Natl. Acad. Sci. U. S. A. 104, 5295–5299.

Zhang, R., Wang, L., Khalizov, A.F., Zhao, J., Zheng, J., McGraw, R.L., Molina, L.T., 2009. Formation of nanoparticles of blue haze enhanced by anthropogenic pollution. Proc. Natl. Acad. Sci. U. S. A. 106, 17650–17654. http://dx.doi.org/10.1073/pnas.0910125106.

Zhang, R., Khalizov, A.F., Wang, L., Hu, M., Xu, W., 2012. Nucleation and growth of nanoparticles in the atmosphere. Chem. Rev. 112, 1957–2011. http://dx.doi.org/10.1021/cr2001756.

Zhao, J., Levitt, N.P., Zhang, R., 2005a. Heterogeneous chemistry of octanal and 2,4-hexadienal with sulfuric acid. Geophys. Res. Lett. 32, L09802. http://dx.doi.org/10.1029/2004GL022200.

Zhao, J., Zhang, R., Misawa, K., Shibuya, K., 2005b. Experimental product study of the OH-initiated oxidation of m-xylene. J. Photochem. Photobiol. A 176, 199–207.

Zheng, J., Zhang, R., Garzón, J.P., Huertas, M.E., Levy, M., Ma, Y., Torres–Jardón, R., Ruiz-Suárez, L.G., Russell, L., Takahama, S., Tan, H., Li, G., Molina, L.T., 2013a. Measurements of formaldehyde at the U.S.–Mexico border during the Cal-Mex 2010 air quality study. Atmos. Environ. 70, 513–520. http://dx.doi.org/10.1016/J.Atmosenv.2012.09.041ss.

Zheng, J., Garzón, J.P., Huertas, M.E., Zhang, R., Levy, M., Ma, Y., Huertas, J.I., Jardón, R.T., Ruíz, L.G., Tan, H., Molina, L.T., 2013b. Volatile organic compounds in Tijuana during the Cal-Mex 2010 campaign: measurements and source apportionment. Atmos. Environ. 70, 521–531. http://dx.doi.org/10.1016/j.atmosenv.2012.11.030.

Zielinska, B., Fujita, E.M., 2003. Characterization of ambient volatile organic compounds at the western boundary of the SCOS97-NARSTO modeling domain. Atmos. Environ. 37, 171–180. http://dx.doi.org/10.1016/S1352-2310(03)00389-3.